



This is a repository copy of *Assisted extraction of the energy level spacings and lever arms in direct current bias measurements of one-dimensional quantum wires, using an image recognition routine.*

White Rose Research Online URL for this paper:  
<http://eprints.whiterose.ac.uk/88066/>

Version: Accepted Version

---

**Article:**

Lesage, A.A.J., Smith, L.W., Al-Taie, H. et al. (7 more authors) (2015) Assisted extraction of the energy level spacings and lever arms in direct current bias measurements of one-dimensional quantum wires, using an image recognition routine. *Journal of Applied Physics*, 117. 015704 . ISSN 0021-8979

<https://doi.org/10.1063/1.4905484>

---

**Reuse**

Unless indicated otherwise, fulltext items are protected by copyright with all rights reserved. The copyright exception in section 29 of the Copyright, Designs and Patents Act 1988 allows the making of a single copy solely for the purpose of non-commercial research or private study within the limits of fair dealing. The publisher or other rights-holder may allow further reproduction and re-use of this version - refer to the White Rose Research Online record for this item. Where records identify the publisher as the copyright holder, users can verify any specific terms of use on the publisher's website.

**Takedown**

If you consider content in White Rose Research Online to be in breach of UK law, please notify us by emailing [eprints@whiterose.ac.uk](mailto:eprints@whiterose.ac.uk) including the URL of the record and the reason for the withdrawal request.



[eprints@whiterose.ac.uk](mailto:eprints@whiterose.ac.uk)  
<https://eprints.whiterose.ac.uk/>

# Assisted extraction of the energy level spacings and lever arms in DC bias measurements of one-dimensional quantum wires, using an image recognition routine

A. A. J. Lesage,<sup>1,\*</sup> L. W. Smith,<sup>1,†</sup> H. Al-Taie,<sup>1,2</sup> P. See,<sup>3</sup> J. P. Griffiths,<sup>1</sup> I. Farrer,<sup>1</sup> G. A. C. Jones,<sup>1</sup> D. A. Ritchie,<sup>1</sup> M. J. Kelly,<sup>1,2</sup> and C. G. Smith<sup>1</sup>

<sup>1</sup>*Cavendish Laboratory, Department of Physics, University of Cambridge, J. J. Thomson Avenue, Cambridge, CB3 0HE, United Kingdom*

<sup>2</sup>*Centre for Advanced Photonics and Electronics, Electrical Engineering Division, Department of Engineering, 9 J. J. Thomson Avenue, University of Cambridge, Cambridge CB3 0FA, United Kingdom*

<sup>3</sup>*National Physical Laboratory, Hampton Road, Teddington, Middlesex TW11 0LW, United Kingdom*

(Dated: December 16, 2014)

A multiplexer technique is used to individually measure an array of 256 split gates on a single GaAs/AlGaAs heterostructure. This results in the generation of large volumes of data, which requires the development of automated data analysis routines. An algorithm is developed to find the spacing between discrete energy levels, which form due to transverse confinement from the split gate. The lever arm, which relates split gate voltage to energy, is also found from the measured data. This reduces the time spent on the analysis. Comparison with estimates obtained visually show that the algorithm returns reliable results for subband spacing of split gates measured at 1.4 K. The routine is also used to assess DC bias spectroscopy measurements at lower temperatures (50 mK). This technique is versatile and can be extended to other types of measurements. For example, it is used to extract the magnetic field at which Zeeman-split 1D subbands cross one another.

Keywords: data extraction, DC bias spectroscopy, one-dimensional transport, GaAs/AlGaAs, semiconductors

## I. INTRODUCTION

It is highly desirable to increase the number of nanostructure devices on a single semiconductor chip, for high throughput testing. This is particularly the case for research into devices for spintronic applications [1, 2] or quantum information processing [3, 4], where often the candidate devices are individual, ‘one-off’ units. In order to move into the realm of computing, it is necessary to fabricate many devices and consider the yield and reproducibility of characteristics.

The split gate is the simplest form of nanostructure device [5]. It can be used to define a one-dimensional (1D) quantum wire in a two-dimensional electron gas (2DEG). At low temperatures ( $T < 4$  K), the conductance  $G$  through the device is quantized in steps of  $G_0 = 2e^2/h$  as a function of the voltage  $V_g$  applied to the split gate [6–9].

In a previous study, 256 split gates were measured in a single cooldown using a multiplexing technique [10, 11]. A large amount of data is generated, and automated data extraction routines are necessary to systematically analyze the data. Therefore, a technique to assess DC bias spectroscopy measurements from an array of split gates is presented here. The routine estimates both the 1D subband spacing and a lever arm relating the voltage scale to an equivalent energy. The data extracted automatically

is compared to data estimated visually by seven users. The routine is versatile and can be applied in other situations. For example, it is used to extract the magnetic field at which Zeeman-split 1D subbands cross one another.

Data are obtained from split gates fabricated on a modulation-doped GaAs/AlGaAs heterostructure, for which the carrier density and mobility are  $2.0 \times 10^{11} \text{ cm}^{-2}$  and  $1 \times 10^6 \text{ cm}^2 \text{ V}^{-1} \text{ s}^{-1}$ , respectively. The 2DEG forms 90 nm below the wafer surface. The split gates have different geometries (the length  $L$  over width  $W$  ratios in  $\mu\text{m}$  are 0.4/0.4, 0.7/0.4 and 1.3/0.4). They are defined by electron-beam lithography, and metalized by thermally evaporating Ti/Au. A two-terminal, constant voltage technique is used to measure  $G$  through the split gates as a function of  $V_g$ , using an AC excitation voltage of 100  $\mu\text{V}$  at 17 Hz. These measurements are performed at  $T = 1.4$  K.

The subband spacings  $\Delta E_{i,i+1}$  and the lever arms  $\alpha_i = \partial V_{\text{dc}} / \partial V_g$  (where  $i$  refers to the 1D subband index) depend directly on the 1D confining potential [8]. They can be estimated by plotting the transconductance  $\Gamma = \partial G / \partial V_g$  against the DC bias voltage  $V_{\text{dc}}$  and  $V_g$ , as shown in Fig. 1(a)-(b) [12–15]. In the greyscale, the dark and light regions correspond to high and low  $\Gamma$ , respectively. As the DC bias voltage becomes more negative, the source and drain chemical potentials ( $\mu_s$  and  $\mu_d$ , respectively), are offset by  $eV_{\text{dc}}$ . The regions of high  $\Gamma$  at  $V_{\text{dc}} = 0$  [points 1R, 2R and 3R in Fig. 1(b), corresponding to the first, second and third 1D subbands], split into two arms as  $V_{\text{dc}}$  is made more negative [see the two dotted lines in Fig. 1(b)]. The  $\Delta E_{i,i+1}$  and  $\alpha_i$  can be directly

\* arthur.lesage@cern.ch

† lws22@cam.ac.uk

FIG. 1. (a)-(b) Greyscale diagrams showing the transconductance  $\Gamma = \partial G / \partial V_g$  as a function of  $V_{dc}$  and  $V_g$ . The dark and light regions correspond to high and low  $\Gamma$ , respectively (white regions therefore indicate plateaus in  $G$ ). Panel (a) shows the measured data after scaling the  $V_{dc}$  axis to correct for series resistance. (b) As  $V_{dc}$  becomes more negative, the lines of high transconductance split into two arms from points 1R, 2R, and 3R, and converge at points 1L, 2L and 3L. One such splitting is indicated by the two yellow dashed lines (for the first 1D subband). The 1D subband spacings  $\Delta E_{1,2}$ ,  $\Delta E_{2,3}$ , and  $\Delta E_{3,4}$  are given by  $V_{dc}$  at points 1L, 2L, and 3L, respectively. The white regions labeled A, B, C, D and E correspond to plateaus at  $0.25$ ,  $1$ ,  $1.5$ ,  $2$ , and  $2.5G_0$ , respectively. The lever arm  $\alpha = \partial V_{dc} / \partial V_g$  can be calculated for each subband. This is illustrated for the second subband:  $\alpha_2 = b/a$ , where  $a$  and  $b$  are shown on the greyscale.

FIG. 2. From (a) to (g), the panels describe the procedure to prepare a matrix of data for evaluation. This culminates with a final matrix at (g) which contains the *islands*; this is subsequently used to find the *crossings*. The red lines indicate where the matrix is divided into sub-matrices. In step (d), only a specific number of data points are retained within each sub-matrix. The matrix in (g) is further divided in two sub-matrices  $\mathcal{M}_L$  and  $\mathcal{M}_R$ , which are searched to find the left and right crossings, respectively.

calculated from the coordinates of the crossings.

The conductance data are corrected for series resistance, which is systematically defined as  $R = G_e^{-1}$  at  $V_g = 0$  for each split gate, where  $G_e$  is the conductance measured. It is also necessary to correct the measured DC bias voltage for series resistance to find the true DC voltage across the device. This article follows the method described in the supplementary information of Ref. [16]: the corrected DC bias voltage is given by  $V_{dc} = V_e - \int_0^{V_e} G_e(V_g, V) R dV$ , where  $V_e$  and  $V$  are the measured DC bias voltage. This correction gives rise to the curve in the left border of the greyscales diagrams (see Fig. 1). The input-offset bias of the current pre-amplifier is negligible.

## II. THE AUTOMATED DATA EXTRACTION ROUTINE

The automated extraction is based on the search for regions of large  $\Gamma$ , since visually,  $\Delta E_{i,i+1}$  are found by locating where lines of high  $\Gamma$  cross. In the following section, the method used to automatically extract  $\Delta E_{i,i+1}$  and  $\alpha_i$  is outlined.

### A. Forming the islands

In order to isolate the crossings [1L, 1R, 2L, 2R, 3L and 3R in Fig. 1(b)], the areas corresponding to low  $\Gamma$  are set to zero, such that only regions where the crossings occur remain. These remaining regions are called *islands*. The different steps needed to form the islands are represented in Fig. 2.

The initial matrix containing the  $\Gamma$  values (step a) can be filtered to improve the extraction (step b). This was not needed for the high  $T$  data. In step c, the matrix is divided horizontally in sub-matrices, where one crossing is expected to occur in each sub-matrix (except at low  $V_g$ ). Only a certain number of points (highest  $\Gamma$ ) are retained in each sub-matrix: the other points are set to 0. This is referred to as the zeroing process, and the remaining points form islands. The division in sub-matrices is important since  $\Gamma$  is higher at low  $V_g$  (bottom of the matrix), and zeroing the unified matrix would result in discarding points at high  $V_g$  (top of the matrix). The zeroed sub-matrices are then gathered (step e), and the resulting matrix can be filtered (step f). Finally, the matrix is cut in two matrices ( $\mathcal{M}_L$  and  $\mathcal{M}_R$ ). This cut is useful because  $\mathcal{M}_L$  and  $\mathcal{M}_R$  can be searched separately to find the left and right crossings, respectively. These two matrices are triangular and the coordinates of the three points for each matrix can be specified.

The preparation of data is very important since the

FIG. 3. (a) Procedure to locate the crossing points of lines of high transconductance. Each horizontal line in triangular matrix  $\mathcal{M}_L$  (constant  $V_g$ ), is scanned from right-to-left (indicated by the horizontal arrow). This process begins from low  $V_g$  to high  $V_g$  (towards zero, as indicated by the vertical arrow). When a non-zero element is found, this suggests a potential new island is located and a test matrix is created represented by the rectangle. Upon further line scans, the dimensions of this island are updated if more non-zero elements are found. The region is considered an island if the test matrix contains more than a certain number of non-zero elements. The end of an island is reached if consecutive line scans contain too few non-zero elements. Islands which occur within a threshold  $V_g$  are merged, as highlighted by the brace. The dotted line shows the right limit of  $\mathcal{M}_L$ . (b) Procedure to locate the transitions between plateaus at  $V_{dc} = 0$ . The matrix  $\mathcal{M}_R$  is scanned line by line (from low  $V_g$  to high  $V_g$ ), as indicated by the vertical arrows. Each line is scanned from right ( $V_{dc} = 0$ ) to left (negative  $V_{dc}$ ), shown by the horizontal arrows. If a non-zero element is found, the line is checked further until a zero element is located or the  $V_{dc}$  limit is reached (represented by the vertical dashed line). If the line has enough non-zero elements, it is added to the current island and its dimensions are stored. Two islands which occur within a threshold  $V_g$  are merged, as highlighted by the brace.

FIG. 4. (a) Final greyscale showing the crossing points and their errors after the results have been validated. The crossings are linked (green lines) to highlight the evolution of 1D subbands with  $V_{dc}$ . The lower left island is not a crossing, but the coordinates are used to calculate  $\alpha_1$ . (b) Evolution of the peaks in the transconductance with  $V_{dc}$  and  $V_g$  (green lines). The parameters needed to estimate the 1D subband spacing  $\Delta E_{i,i+1}$  and lever arm  $\alpha_i$  are shown, along with the associated errors. The left (right) crossing points and their coordinates are represented by the red (blue) dots, and error bars are marked by + (as an example, the arrows highlight the errors  $\delta V_{dc3}^L$ ,  $\delta V_{g3}^L$ , and  $\delta V_{g3}^R$ ). The slopes of the green lines  $\gamma_i^L$  and  $\gamma_i^R$  are used to calculate  $\alpha_i$ .

quality of the islands is highly dependent on this process. Several parameters can be adjusted such as the filtering processes (steps b and f), the number of sub-matrices to be created after slicing (step c), the number of remaining points after the zeroing process for each sub-matrix (step d), the geometries of  $\mathcal{M}_L$  and  $\mathcal{M}_R$  (step g, these geometries have the biggest impact on the extraction). The algorithm includes a built-in assisted calibration routine, which allows the user to select optimal parameters on a greyscale representative of the data to be analyzed.

Once the data is suitably prepared, the next part of the algorithm locates the islands. The crossings are assumed to occur in the middle of each island found. The associated errors are defined as the dimensions of the islands.

### B. The right crossings

The right crossings [1R, 2R and 3R of Fig. 1(b)] are extracted first, because they occur at  $V_{dc} = 0$ , and are therefore easier to locate. The process is described in Fig. 3(b). The crossings are searched from low  $V_g$  to

high  $V_g$  (bottom-to-top). If a non-zero element [dark in Fig. 3(b)] is found at  $V_{dc} = 0$ , the line (constant  $V_g$ ) is then searched from  $V_{dc} = 0$  to more negative  $V_{dc}$  (right-to-left). The algorithm checks whether there are more non-zero elements on this line [the lower  $V_{dc}$  limit to which non-zero elements are searched is highlighted by the vertical dotted line in Fig. 3(b)]. If a certain number of elements is found, the line is added to the island, otherwise, the island is terminated. If two islands are found to be very close, they are merged.

Three parameters can be customized: the number of lines jumped after an island is terminated, the lower  $V_{dc}$  limit to which the lines are scanned, and the minimum number of non-zeros elements in a single line for it to be added to the island.

### C. The left crossings

Next, the left crossings [1L, 2L and 3L of Fig. 1(b)] are extracted. The process is pictured in Fig. 3(a). Each line (constant  $V_g$ ) is inspected from the lower  $V_{dc}$  limit of  $\mathcal{M}_L$  [red dashed line in Fig. 3(a)] to more negative  $V_{dc}$

FIG. 5. Comparison between automated and visual extractions of the subband spacings  $\Delta E_{i,i+1}$  [panels (a)-(c)] and the lever arms  $\alpha_i$  [panels (d)-(e)]. Data were estimated visually by seven people. The data point shows the mean estimate and the error bar shows the standard deviation. Dashed lines indicate the one-to-one correspondence of the axes. The correlation between visual and automated extractions are quantified by the Pearson product-moment coefficients: (a)  $r = 0.72$  ( $\Delta E_{1,2}$ ), (b)  $r = 0.02$  ( $\Delta E_{2,3}$ ), (c)  $r = 0.36$  ( $\Delta E_{3,4}$ ), (d)  $r = 0.78$  ( $\alpha_1$ ), (e)  $r = 0.73$  ( $\alpha_2$ ) and (f)  $r = 0.28$  ( $\alpha_3$ ).

FIG. 6. Automated data extraction routine applied to two alternative data sets, from a different device measured in a dilution refrigerator with a base temperature of 50 mK. Panel (a) shows the DC bias spectroscopy, in which transconductance  $\Gamma$  is plotted as a function of  $V_g$  and  $V_{dc}$ . Lines of high  $\Gamma$  are well defined at this  $T$ , therefore the error bars of the estimate are reduced. (b) Transconductance  $\Gamma$  as a function of  $V_g$  and magnetic field  $B$  (at  $V_{dc} = 0$ ). Lines of high  $\Gamma$  diverge from  $B = 0$ , due to the spin-splitting of 1D subbands. The automated routine can be used to estimate the crossing points of these lines at low  $B$ , illustrating the versatility of this method. This is despite the curvature of these lines which arises due to the diamagnetic shift of 1D subbands. Note that the transformation  $B \rightarrow -B$  has been applied, so that right crossings occur at  $B = 0$ .

(the search begins at low  $V_g$ ). When a non-zero element is found, a test matrix including the surrounding points is created [represented by red rectangles in Fig. 3(a)]. If the test matrix contains a certain number of non-zero elements, it is assumed that a new island has been found. Matrix  $\mathcal{M}_L$  is then scanned line by line and the edges of the island ( $V_{dc}$  and  $V_g$  bounds) are updated until the island is terminated (which occurs if a certain number lines with insufficient non-zero elements are found consecutively). If two islands are found to be very close, they are merged.

The data are searched in a way such that a left island is always located at higher  $V_g$  than the corresponding right island. This condition can be removed depending on the data, but is necessary for DC bias spectroscopy (a left crossing always result from the splitting of a right crossing). Note that the bottom left island in Fig. 4(a)-(b) is found by the algorithm: it does not correspond to any crossing, but the coordinates of the island are necessary to calculate  $\alpha_1$ .

Five parameters can be customized: the length and the width of the test matrix, the minimum number of non-zero elements a test matrix should contain in order for a new island to be located, the  $V_g$  limit below which two islands are merged, and the maximum number of consecutive lines without enough non-zero elements before an island is terminated.

#### D. Validation of the results

In order to make the routine as robust as possible, the user is asked to validate the results. A temporary plot is displayed and the user can accept or propose a new numerical value for the scale  $s$  (increasing  $s$  makes the islands easier to find, but artifacts may be mistaken for islands). In case the number of left ( $n_L$ ) and right ( $n_R$ ) crossing points located do not satisfy  $n_L \leq n_R$ , islands may have been missed and a noisy option can be enabled to make the definition of islands less stringent. A final output is displayed with the validated results, in which the crossings are linked, as shown in Fig. 4(a). The variables shown on the plot are used to calculate  $\Delta E_{i,i+1}$  and  $\alpha_i$  via the following equations:

$$\Delta E_{i,i+1} = -eV_{dc}^L, \quad \alpha_i = \frac{1}{\gamma_i^\uparrow + \gamma_i^\downarrow},$$

$$\gamma_i^\uparrow = \frac{V_{g,i}^R - V_{g,i}^L}{V_{dc,i}^L}, \quad \gamma_i^\downarrow = \frac{V_{g,i-1}^L - V_{g,i}^R}{V_{dc,i-1}^L},$$

with L and R referring to left and right sides, respectively. To calculate  $\alpha_i$ , the intermediate variables  $\gamma_i$  are used. They correspond to the slopes of the two crossing curves on the greyscale, as shown in Fig. 4(b).

### III. COMPARISON OF THE RESULTS

The algorithm was used to estimate  $\Delta E_{i,i+1}$  and  $\alpha_i$  for subbands 1, 2 and 3 from 13 split gates of different geometries, measured during the same cooldown [17]. The extraction routine required only a single calibration step in order to find subband spacings for all the devices (the input parameters are the same for all split gates despite the different geometries).

The extraction was also carried out visually by seven people, and Fig. 5 shows the comparison between automated data (the error bars are set to half the values calculated) and visual data (the data point corresponds to the mean estimate and the error bar shows the standard deviation). The red dotted line represents the function  $x = y$  to facilitate comparison. The Pearson product-moment correlation coefficient  $r$  is calculated for each variables ( $r$  is close to 1 for high correlation and close to 0 for no correlation): (a)  $r = 0.72$  ( $\Delta E_{1,2}$ ), (b)  $r = 0.02$  ( $\Delta E_{2,3}$ ), (c)  $r = 0.36$  ( $\Delta E_{3,4}$ ), (d)  $r = 0.78$  ( $\alpha_1$ ), (e)  $r = 0.73$  ( $\alpha_2$ ) and (f)  $r = 0.28$  ( $\alpha_3$ ).

The spread in estimated values using the routine is much smaller than estimates obtained visually. Wide variations of visual extractions reflects the divergence of opinions on how to define a crossing. For  $\Delta E_{1,2}$  [Fig. 5(a)], the correlation is highest since the first crossing occurs at low  $V_g$  and is often better resolved in greyscales compared to the second and third crossings. The error bars associated with visual extractions are also larger for  $\Delta E_{2,3}$  and  $\Delta E_{3,4}$ , showing the extraction becomes more difficult for higher subbands.

Visual  $\Delta E_{i,i+1}$  estimates are often higher than automated ones because the algorithm selects the center of the islands, while visually users often select the left part of the island, which occurs at lower  $V_{dc}$ . The automated values of  $\alpha_i$  agree reasonably well with visual estimates. Since  $\alpha_i$  is calculated from a slope, it is much more sensitive to variations than  $\Delta E_{i,i+1}$  (therefore the error bars are quite large). The algorithm tends to return a lower  $\alpha_i$  than visual extraction (especially for higher subbands). The automated extractions are not always within the visual error bars in Fig. 5, since the error bars show the standard deviation of the visual estimate. However, the automated data points are within (or close to) the maximum and minimum values of the visual estimates.

### IV. APPLICATION TO OTHER MEASUREMENTS

In order to show the versatility of the routine, it was tested on two other sets of data from a different split gate [18]. This device was measured at the lower temperature  $T = 50$  mK in a dilution refrigerator, with and without an in-plane magnetic field  $B$ . Figures 6(a)-(b) show the results of the crossing extraction routine on these two sets of data.

### A. Low temperature data

Figure 6(a) shows DC bias spectroscopy data at  $T = 50$  mK. At this  $T$ , features related to quantum coherence – such as the quantized  $G$  plateaus – are better defined [8]. The lines in the greyscale become much better defined and the estimates of  $\Delta E_{i,i+1}$  and  $\alpha_i$  are more accurate. When applying the routine, the data had to be filtered to diminish the influence of secondary crossings: transitions between  $G$  plateaus are so well defined that the arms of high  $\Gamma$  cross several times at lower  $V_{dc}$ .

The number of sub-matrices used to ‘zero’ the data [see Fig. 2(c)] had to be increased (from six to seven because more subbands were fully resolved). The bounds of  $\mathcal{M}_L$  and  $\mathcal{M}_R$  had to be redefined, since the crossings occur at higher  $V_{dc}$ . After these modifications (calibration), the algorithm can be used to extract crossings of many devices measured in similar conditions.

### B. Magnetic field data

Figure 6(b) shows the transconductance  $\Gamma$  as a function of  $B$  and  $V_g$ . In the presence of  $B$ , the spin degeneracy of 1D subbands is lifted [9], and crossings are observed on the greyscale (in this case, these crossings are the filling of spin-split subbands; different to DC bias spectroscopy where the 1D subbands do not split but pass through  $\mu_s$  and  $\mu_d$  alternately). This required the transformation  $B \rightarrow -B$ . The lines of high  $\Gamma$  are curved due to the effect of  $B$  on the overall confining potential in the 1D wire and 2DEG. This did not prevent the algorithm from correctly identifying the crossings. Seven sub-matrices were used for zeroing the data [see Fig. 2(c)] and the parameters were adjusted as described previously.

## V. SUMMARY

A technique for automated data extraction from quantum systems has been presented. This was specifically applied to estimate the 1D subband spacings and lever arms from DC bias measurements of split-gate devices measured at  $T = 1.4$  K.

The method is faster than performing the task visually (typically three times faster compared to an assisted visual extraction), and provides a systematic extraction along with symmetrical error bars. The input parameters of the algorithm are easily alterable, and different types of data can be assessed using this technique. For example, the algorithm was tested on DC bias data measured at lower temperatures, and on magnetic field data to assess the Zeeman splitting of 1D subbands.

Algorithms for automated data analysis are important in the move towards measuring large numbers of devices, for yield analysis and statistical studies. The method presented is widely applicable, and can be used to locate

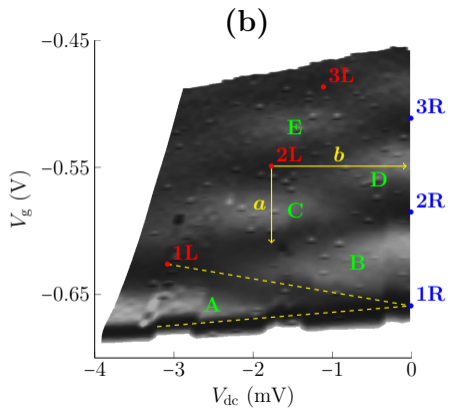
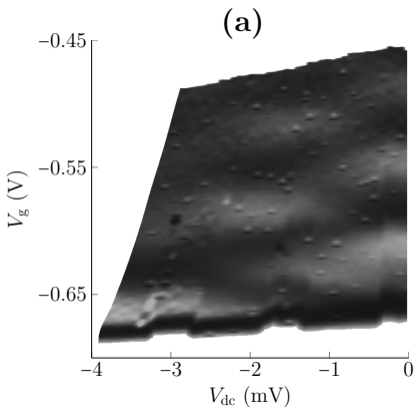
points of interest in data where these points are represented by high data values. For example, in measurements of quantum dots this approach can be used to find crossing points of Coulomb diamonds, to estimate the spacing of the energy levels [19]. Additionally, this routine may be used to locate triple points in charge stability diagrams of double quantum dots [20].

## ACKNOWLEDGMENTS

This work was supported by the Engineering and Physical Sciences Research Council grant No. EP/IO14268/1.

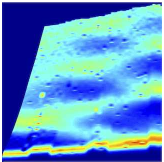
The authors would like to thank R. D. Hall for electron-beam exposure, and C. Chen, A. Klimont, C. H. Chong, R. K. Puddy, Z. Dou for visually estimating the crossings on greyscale.

- 
- [1] D. D. Awschalom and M. E. Flatté. Challenges for semiconductor spintronics. *Nature Physics*, 3(3):153–159, March 2007.
- [2] D. Awschalom and N. Samarth. Spintronics without magnetism. *Nature Physics*, 2(2):50, June 2009.
- [3] C. Kloeffer and D. Loss. Prospects for spin-based quantum computing in quantum dots. *Annual Review of Condensed Matter Physics*, 4(1):51–81, April 2013.
- [4] F. A. Zwanenburg, A. S. Dzurak, A. Morello, M. Y. Simmons, L. C. L. Hollenberg, G. Klimeck, S. Rogge, S. N. Coppersmith, and M. A. Eriksson. Silicon quantum electronics. *Reviews of Modern Physics*, 85(3):961–1019, July 2013.
- [5] T. J. Thornton, M. Pepper, H. Ahmed, D. Andrews, and G. J. Davies. One-dimensional conduction in the 2D electron gas of a GaAs-AlGaAs heterojunction. *Physical Review Letters*, 56(11):1198–1201, 1986.
- [6] R. Landauer. Spatial variation of currents and fields due to localized scatterers in metallic conduction. *IBM Journal of Research and Development*, 1(3):223, 1957.
- [7] L. I. Glazman, G. B. Lesovik, D. E. Khmel'nitskii, and R. I. Shekhter. Reflectionless quantum transport and fundamental ballistic-resistance steps in microscopic constrictions. *JETP Letters*, 48(4):238–241, 1988.
- [8] M. Büttiker. Quantized transmission of a saddle-point constriction. *Physical Review B*, 41(11):7906–7909, 1990.
- [9] D. A. Wharam, T. J. Thornton, R. Newbury, M. Pepper, H. Ahmed, J. E. F. Frost, D. G. Hasko, D. C. Peacock, D. A. Ritchie, and G. A. C. Jones. One-dimensional transport and the quantisation of the ballistic resistance. *Journal of Physics C*, 21(8):209–214, 1988.
- [10] H. Al-Taie, L. W. Smith, B. Xu, P. See, J. P. Griffiths, H. E. Beere, G. A. C. Jones, D. A. Ritchie, M. J. Kelly, and C. G. Smith. Cryogenic on-chip multiplexer for the study of quantum transport in 256 split-gate devices. *Applied Physics Letters*, 102(243102):1–4, 2013.
- [11] L. W. Smith, H. Al-Taie, F. Sfigakis, P. See, A. A. J. Lesage, B. Xu, J. P. Griffiths, H. E. Beere, G. A. C. Jones, D. A. Ritchie, M. J. Kelly, and C. G. Smith. Statistical study of conductance properties in one-dimensional quantum wires focusing on the 0.7 anomaly. *Physical Review B*, 90(4):045426, July 2014.
- [12] N. K. Patel, J. T. Nicholls, L. Martín-Moreno, M. Pepper, J. E. F. Frost, D. A. Ritchie, and G. A. C. Jones. Evolution of half plateaus as a function of electric field in a ballistic quasi-one-dimensional constriction. *Physical Review B*, 44(24):13549–13555, 1991.
- [13] T.-M. Chen, A. C. Graham, M. Pepper, I. Farrer, and D. A. Ritchie. Bias-controlled spin polarization in quantum wires. *Appl. Phys. Lett.*, 93(032102):1–3, 2008.
- [14] T.-M. Chen, A. C. Graham, M. Pepper, I. Farrer, D. Anderson, G. A. C. Jones, and D. A. Ritchie. Direct observation of nonequilibrium spin population in quasi-one-dimensional nanostructures. *Nano Letters*, 10(7):2330–2334, 2010.
- [15] K. J. Thomas, M. Y. Simmons, J. T. Nicholls, D. R. Mace, M. Pepper, and D. A. Ritchie. Ballistic transport in one-dimensional constrictions formed in deep two-dimensional electron gases. *Applied Physics Letters*, 67(109), August 1995.
- [16] A. Srinivasan, L. A. Yeoh, O. Klochan, T. P. Martin, J. C. H. Chen, A. P. Micolich, A. R. Hamilton, D. Reuter, and A. D. Wieck. Using a tunable quantum wire to measure the large out-of-plane spin splitting of quasi two-dimensional holes in a GaAs nanostructure. *Nano Letters*, 13:148–152, 2012.
- [17] Although more split gates were measured on this chip during the cooldown, many showed effects of disorder due to a large split gate length ( $L$ ) and width ( $W$ ), making it more likely to encounter an impurity in the 1D channel ( $L/W$  up to 1.3/0.6  $\mu\text{m}$  were measured). These data were therefore not included in the analysis, since the disorder prevented even a visual extraction of the subband spacings.
- [18] L. W. Smith, W. K. Hew, K. J. Thomas, M. Pepper, I. Farrer, D. Anderson, G. A. C. Jones, and D. A. Ritchie. Row coupling in an interacting quasi-one-dimensional quantum wire investigated using transport measurements. *Physical Review B*, 80(4):041306, July 2009.
- [19] R. Hanson, L. P. Kouwenhoven, J. R. Petta, S. Tarucha, and L. M. K. Vandersypen. Spins in few-electron quantum dots. *Reviews of Modern Physics*, 79(4):1217–1265, October 2007.
- [20] W. G. van der Wiel, S. De Franceschi, J. M. Elzerman, T. Fujisawa, S. Tarucha, and L. P. Kouwenhoven. Electron transport through double quantum dots. *Reviews of Modern Physics*, 75(1):1–22, December 2002.

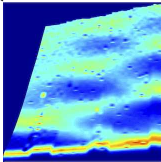




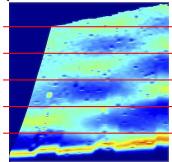
(a) Filtering



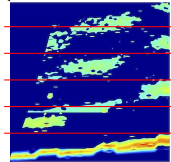
(b) Slicing



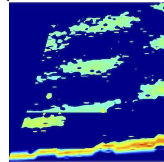
(c) Zeroing



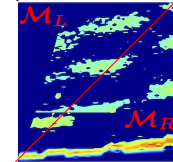
(d) Gathering

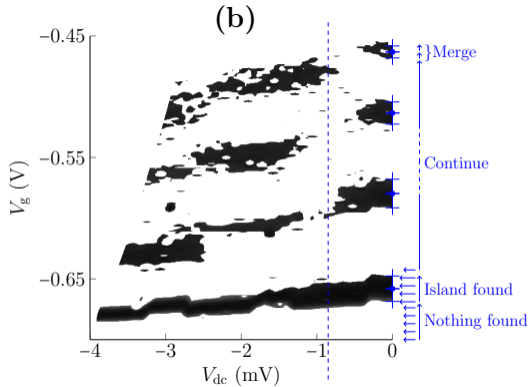
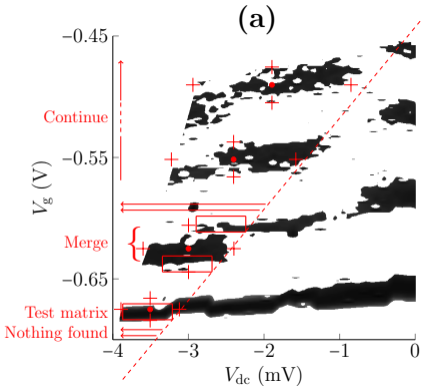


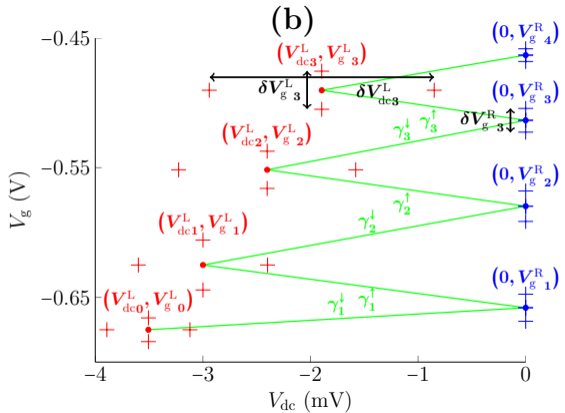
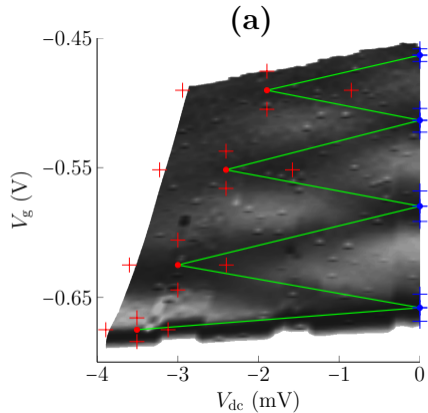
(e) Filtering

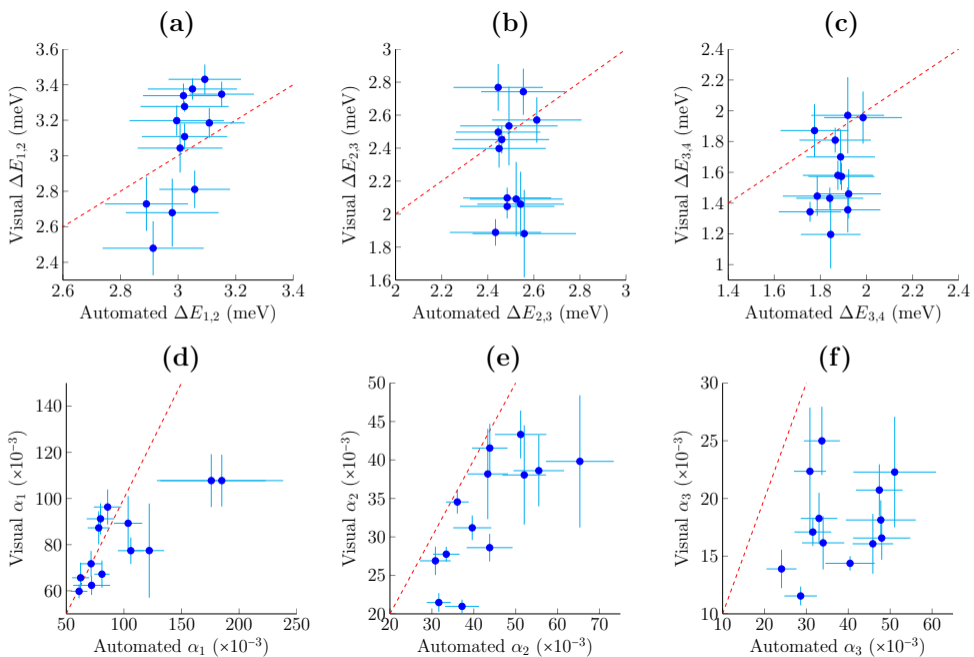


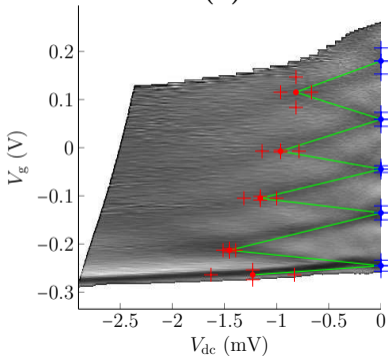
(f) Partitioning









**(a)****(b)**